

Specular Beamforming

Alfonso Rodriguez-Molares, Ali Fatemi, Lasse Løvstakken, and Hans Torp

Abstract—Acoustically hard objects, such as bones, needles, or catheters, are poorly visualized in conventional ultrasound images. These objects behave like acoustic mirrors and reflect sound in specific directions. Soft tissue and diffusive reflectors scatter sound in a broad range of directions. Conventional delay-and-sum beamforming is based on the assumption of a purely scattering domain with relatively weak reflectivity. We present an adaptive beamforming technique that takes into account the physics of specular reflection. Patterns predicted by the law of reflection are detected across the pool of received data and used to enhance the visualization of specular energy. This technique can be applied to any synthetic imaging sequence. Here, it is applied to synthetic transmit aperture imaging. *In vitro* experiments show a clear improvement in target visibility and an increase of 30 to 60 dB in signal-to-noise ratio.

Index Terms—Acoustic beams, biomedical imaging, ultrasonography.

I. INTRODUCTION

THE interaction between waves and surfaces is governed by the relation between wavelength and surface roughness size [1]. If the wavelength is much smaller than the roughness size, then the signal is reflected uniformly on a broad range of directions with random phase, producing an incoherent signal such as the light reflected from matte surfaces. If the wavelength is comparable with the roughness size, then both amplitude and phase become random, leading to the speckle noise observed in ultrasound imaging. If the wavelength is much larger than the roughness size, then energy is reflected in a mirrorlike fashion: the radiation pattern depends on the incidence angle, and the reflected signal keeps its phase after reflection.

Since its beginnings in 1950 ultrasound technology has been developed and optimized to detect scattered energy. Receive apodization and delays are computed based on the assumption that tissue is composed of a collection of point scatterers. It should come as no surprise that objects such as bones, needles, or catheters are often poorly visualized in conventional B-mode images [2], [3]. This is often aggravated by reverberation, speckle noise, and signal dropout [4].

Several factors contribute to this poor visualization. Specular interfaces deflect the ultrasound beam and make invalid the geometrical model used for the calculation of delay

Manuscript received December 28, 2016; accepted May 22, 2017. Date of publication May 26, 2017; date of current version August 28, 2017. This work was supported in part by the Norwegian Research Council (Norges forskningsråd) as part of the project Vertebral Intraoperative Repair by Targeted Ultrasound Imaging, under Project 219326 and in part by the Center for Innovative Ultrasound Solutions. (Corresponding author: Alfonso Rodriguez-Molares.)

The authors are with the Department of Circulation and Medical Imaging, Norwegian University of Science and Technology, 7030 Trondheim, Norway (e-mail: alfonso.r.molares@ntnu.no).

Digital Object Identifier 10.1109/TUFFC.2017.2709038

and apodization. Hard objects, with much higher acoustic impedance than soft tissue, violate the weak reflection assumption. As a result, reflecting boundaries often look distorted and produce ghost interfaces [5].

Even more challenging is the problem of visibility. Point scatterers always reflect part of the energy back to the probe. A point scatterer floating in anechoic medium can always be detected. A specular reflector in front of the probe can be completely invisible if the reflected energy is not directed back to the probe. In some cases, it is physically impossible to detect specular interfaces. Exactly as in some cases, we cannot see our own reflection in a mirror.

This visualization problem hinders some clinical procedures, such as bone registration in surgery [6], guidance for spinal anesthesia [7], or diagnosis of bone fractures in emergency rooms [8]. A correct visualization of specular reflectors is paramount for instrument tracking [9] in medical applications, such as ultrasound-guided biopsies [10], regional anesthesia [11], and fetal blood transfusion [12].

It is well known that spatial compounding [13]–[15] enhances edge visualization. Spatial compounding involves averaging multiple images of the target region over different orientation angles. Due to its simplicity, spatial compounding is available in most diagnostic scanners and has become the reference technique for the visualization of specular reflectors. But some techniques have been proposed to improve upon spatial compounding.

Minimum variance beamforming (MVB) [16], [17] has been shown to provide higher resolution, better interference suppression capability, and edge definition. However, some factors degrade the performance of MVB in practice, such as errors in the steering vector [18]. Mehdizadeh *et al.* [19] showed that eigenspace MVB improved the visibility of bones in water tank experiments, but its performance was severely degraded in the presence of speckle noise. Range point migration [20] improved the visualization of specular interfaces, but the method was mostly suited for convex interfaces. Phase-based feature detection [2] has been used to improve the visibility of reflecting boundaries in medical images. The combination of spatial compounding, template matching, and feature detection by phase symmetry provided good results in a clinical setup [21]. However, the reflector shape must be known *a priori*.

Based on the beam geometry and the location of the peak echo amplitude along the aperture, Bandaru *et al.* [22] estimated the orientation of a planar reflector using the law of reflection and its location by conventional time-of-flight measurement. Estimating the orientation with the location of the peak amplitude is not a robust metric in presence of high levels of speckle noise. In addition, the method does not intro-

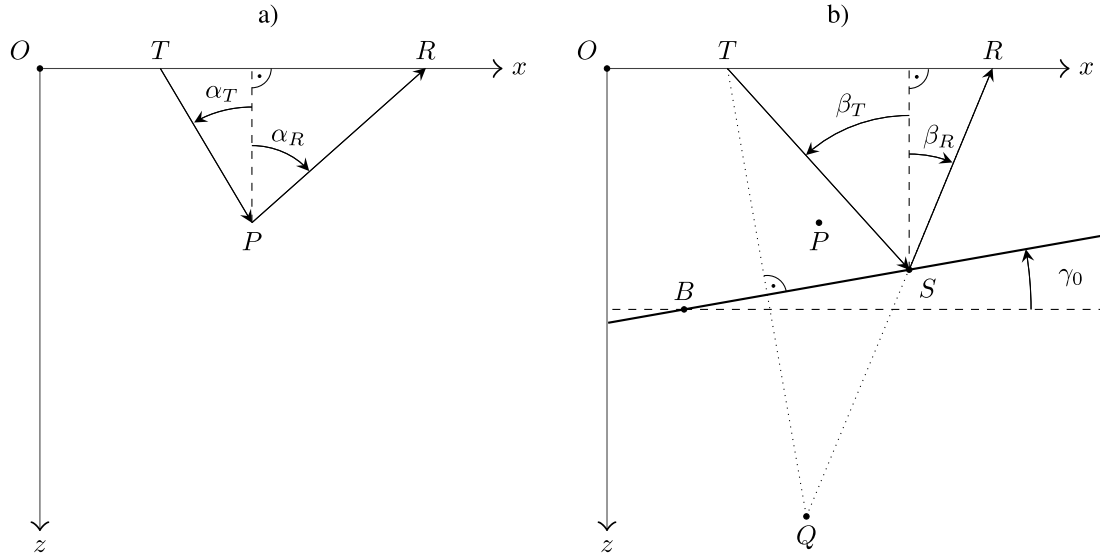


Fig. 1. Geometrical entities used for delay calculation in (a) the assumed path for a signal focused at P and (b) the path that the signal follows in the presence of a planar reflector at B with inclination γ_0 .

duce adaptive steering on transmit. These two problems were addressed by the image source localization (ISL) method [23]. Combining the image source principle and source localization algorithms, ISL extracts the location and orientation of a specular reflector.

Both [22] and [23] were intended for detection only. It was assumed that the reflected signal could be detected within the pool of received channel data. But in case of very low signal-to-noise ratio (SNR), both methods are unable to produce any result, stopping any subsequent analysis, or improvement of the images. In addition, although ISL introduces adaptation of the transmit beams, the signal coherence along the transmit events remained unexploited.

Alternatively to detection, one could develop a beamforming technique tailored to the physics of specular reflection. The specular image could then be assessed by the operator or further improved by additional image processing techniques. Using that approach, we presented in [24] a beamformer based on the law of reflection. By deriving a model for the specular energy reflected by a specular interface, we designed a matched filter that maximizes the specular-to-speckle-energy ratio. The result was an adaptive beamforming method that enhances the visualization of planar interfaces, even when they are buried in speckle noise. Here, we present an extended version of [24] by providing additional analysis and discussion. We also provide new experimental data to validate the theory, and we study the performance of the specular beamformer in needle visualization.

II. THEORY

The scope of this derivation is restricted to planar reflectors. The method can be applied on any imaging technique that makes it possible to coherently compound transmit signals, such as synthetic transmit aperture imaging (STAII) [25], coherent plane-wave compounding [26], synthetic aperture sequential beamforming [27], or diverging wave imaging [28]. Theory and results are presented for STAII and linear probes

only. For simplicity, we assume that the array is placed at $z = 0$. The derivation for other imaging sequences and probe geometries is analogous to the one presented here.

A. Synthetic Transmit Aperture Imaging

A transmitting and a receiving element are placed, respectively, at locations $T \equiv (x_T, 0)$ and $R \equiv (x_R, 0)$. Let us denote as $s(T, R, t)$ the pulse-echo signal from element T to element R . A focal point is set at location $P \equiv (x, z)$ within the focal plane in front of the array. In STAII, the value of the beamformed signal at point P is given by

$$b_{\text{DAS}}(P) = \sum_{\forall T} \sum_{\forall R} s(T, R, t)|_{t=t_{TPR}} \quad (1)$$

where

$$t_{TPR} = \frac{|\overrightarrow{TP}| + |\overrightarrow{PR}|}{c_0} \quad (2)$$

and $|\overrightarrow{TP}|$ and $|\overrightarrow{PR}|$ are, respectively, the distances from T and R to P , and c_0 is the speed of sound. Note that $b(P)$ has no temporal dimension: it is the value of the beamformed signal at point P , also referred to as “pixel value.” For the sake of conciseness hereinafter, we will denote

$$s_{TPR} \equiv s(T, R, t)|_{t=t_{TPR}}. \quad (3)$$

B. Signal Reflected by a Point Scatterer

If a point scatterer lies at point P , and if the temporal effects of the spatial impulse response are neglected, then the pulse-echo signal can be modeled as

$$s(T, R, t) = \frac{d(\alpha_T)}{|\overrightarrow{TP}|} \frac{d(\alpha_R)}{|\overrightarrow{PR}|} e_{2W} \left(t - \frac{|\overrightarrow{TP}| + |\overrightarrow{PR}|}{c_0} \right) \quad (4)$$

where α_T and α_R are, respectively, the transmitting and receiving angles as shown in Fig. 1(a), $d(\cdot)$ is the element directivity function, and

$$e_{2W}(t) = e(t) * \varepsilon_T(t) * \varepsilon_R(t) \quad (5)$$

denotes the two-way pulse, i.e., the convolution of the excitation signal $e(t)$ with the electromechanical impulse responses of both the transmitting and the receiving element $\varepsilon_T(t)$ and $\varepsilon_R(t)$. Assuming that all elements are identical, $e_{2W}(t)$ becomes independent of T and R . For rectangular shaped elements, and for P within the focal plane, the directivity function can be modeled as [29]

$$d(\alpha) = \text{sinc}\left(\frac{a}{\lambda} \sin \alpha\right) \quad (6)$$

where a is the element width, and λ is the wavelength. By inserting (2) into (4), we observe that the value of the delayed pulse-echo signal at P becomes

$$s_{TPR} = \frac{d(\alpha_T)}{|\vec{TP}|} \frac{d(\alpha_R)}{|\vec{PR}|} e_{2W}(0). \quad (7)$$

C. Signal Reflected by a Plane Reflector

Let us assume now that a reflecting surface lies at point $B \equiv (x_B, z_B)$ with orientation γ_0 , as shown in Fig. 1(b). The path followed by the pulse can be calculated using the image source principle, which predicts that the image source $Q \equiv (x_Q, z_Q)$ will be symmetric to T respect to the reflecting plane:

$$Q = 2(B + (\vec{BT} \cdot \vec{D})\vec{D}) - T \quad (8)$$

where \cdot denotes the scalar product, and $D = (\cos \gamma_0, -\sin \gamma_0)$ for a 2-D domain. The reflecting point $S \equiv (x_S, z_S)$ is in the intersection of the reflecting plane and the line \overline{QR} , that is

$$S = B + \vec{D} \left[\frac{z_B - z_Q - \frac{z_Q}{x_Q - x_R}(x_B - x_Q)}{\sin \gamma_0 + \frac{z_Q}{x_Q - x_R} \cos \gamma_0} \right]. \quad (9)$$

Let us define the transmitting and receiving angles as β_T and β_R , as shown in Fig. 1(b). The pulse-echo signal from element T to element R can be modeled as

$$s(T, R, t) = \frac{d(\beta_T) d(\beta_R)}{|\vec{QR}|} e_{2W}\left(t - \frac{|\vec{QR}|}{c_0}\right). \quad (10)$$

Note that the signal amplitude depends on the distance $|\vec{QR}|$, not $|\vec{QS}| |\vec{SR}|$. Contrary to the point scatterer case, where a secondary spherical wave was generated at P , the reflector merely changes the apparent location of the wave produced by the transmit element at T .

Inserting (2) into (10), the value of the delayed pulse-echo signal at P becomes

$$s_{TPR} = \frac{d(\beta_T) d(\beta_R)}{|\vec{QR}|} e_{2W}\left(\frac{|\vec{TP}| + |\vec{PR}| - |\vec{QR}|}{c_0}\right). \quad (11)$$

Comparing (7) and (11), we observe that the propagation delay is compensated only if $|\vec{QR}| = |\vec{TP}| + |\vec{PR}|$. That condition is fulfilled only on a small subset of TPR combinations.

In particular when the specular reflector is at the focal point ($S \equiv P$), we see that $\alpha_T = \beta_T$ and $\alpha_R = \beta_R$. In that case, delays are perfectly compensated only if the law of reflection is fulfilled, i.e., when the incident angle θ_i equals

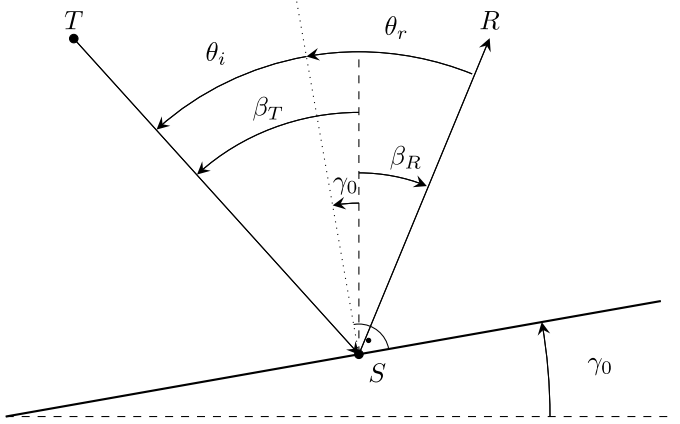


Fig. 2. Relation between the transmit β_T and receive β_R angles and the incident θ_i and reflecting θ_r angles.

the reflecting angle θ_r . Fig. 2 shows the geometrical relation between β_T and θ_i , and β_R and θ_r , which can be written as

$$\theta_i = \beta_T - \gamma \quad (12)$$

$$\theta_r = \beta_R + \gamma \quad (13)$$

and then combined into

$$\beta_T = \beta_R + 2\gamma_0. \quad (14)$$

Any received specular energy must fulfill (14). Notice that if $S \equiv P$, then (14) can also be written as $\alpha_T = \alpha_R + 2\gamma_0$.

D. Specular Transform

For a given P , there is an injective relation between T and α_T , and R and α_R . It is therefore possible to express the values of the delayed pulse-echo signal in terms of the transmit and receive angles α_T and α_R , so that

$$g(P, \alpha_T, \alpha_R) = s_{TPR} \iff \begin{cases} \tan \alpha_T = \frac{x - x_T}{z - z_T} \\ \tan \alpha_R = \frac{x - x_R}{z - z_R}. \end{cases} \quad (15)$$

For those pairs, (α_T, α_R) that do not fulfill (15) the value of $g(P, \alpha_T, \alpha_R)$ can be obtained by linear interpolation.

To illustrate this mapping, Fig. 3 shows the theoretical values of $g(P, \alpha_T, \alpha_R)$ for a 128 elements, 300 μm pitch, linear array. Several scenarios are considered, but in all cases, the focal point is set at $P = (0, 20)$ mm. The array size and the location respect to P determine the range of transmit and receive angles.

Fig. 3(a) shows $g(P, \alpha_T, \alpha_R)$, according to (7), when a point scatterer lies at P . All propagation delays are correctly compensated for and all the values are in phase. The influence of the element directivity and geometrical dispersion is observed as a decaying amplitude with increasing $|\alpha_T|$ and $|\alpha_R|$.

Fig. 3(b) shows $g(P, \alpha_T, \alpha_R)$ when a collection of randomly located point scatterers are in the vicinity of P . This scenario corresponds to what we refer to as speckle noise. In this case, the propagation delays are not correctly compensated. The variance of the signal is highest in the direction $(\alpha_T, -\alpha_R)$, and lowest in the direction (α_T, α_R) .

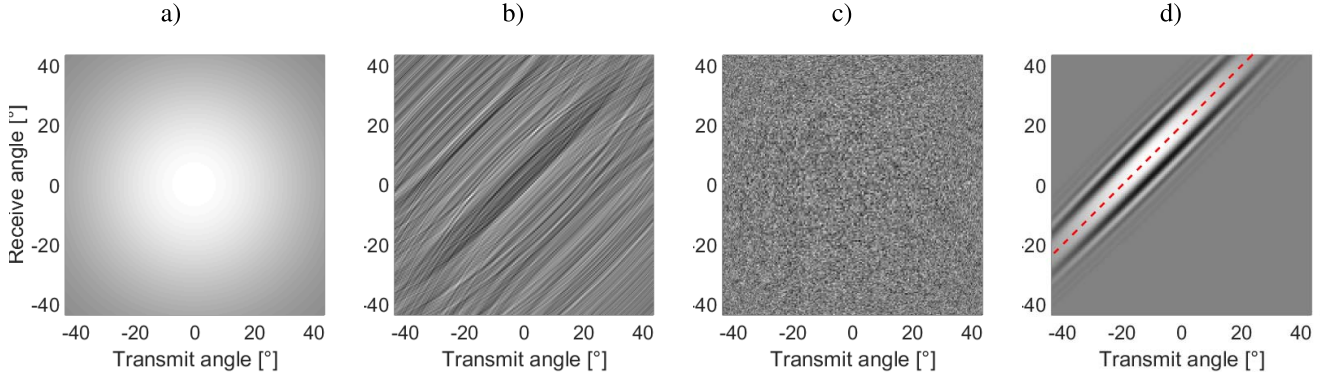


Fig. 3. Delayed signals in terms of α_T and α_R for (a) point scatterer, (b) speckle noise, (c) thermal noise, and (d) plane reflector $\gamma_0 = -10^\circ$. The relation (14) is also plotted in (d) as a dashed red line.

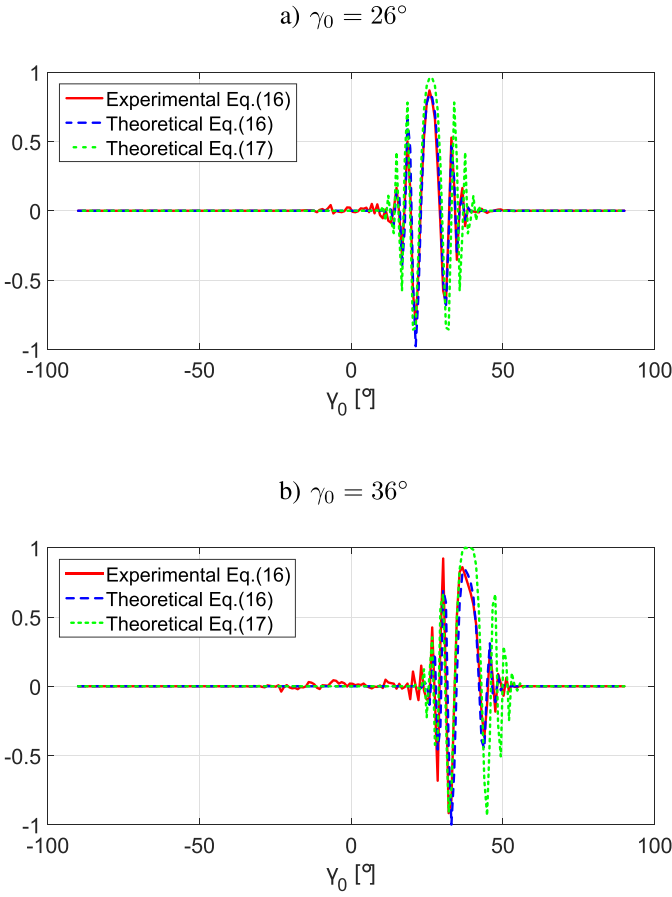


Fig. 4. Experimental validation of the specular transform $f(P, \gamma)$ and model $m(P, \gamma, \gamma_0)$ of the signal received from a needle with inclination (a) $\gamma_0 = 26^\circ$ and (b) $\gamma_0 = 36^\circ$.

Fig. 3(c) shows $g(P, \alpha_T, \alpha_R)$ when Gaussian noise is received by the array, corresponding to a scenario of pure thermal noise. In this case, the variance of the signal is identical in all directions.

Fig. 3(d) shows $g(P, \alpha_T, \alpha_R)$, according to (11), when a planar reflector with inclination $\gamma_0 = -10^\circ$ lies at P . As in the speckle noise scenario, the signal values are highly correlated in the direction (α_T, α_R) . It is observed that the values of $g(P, \alpha_T, \alpha_R)$ are nearly symmetric respect to (14). Equation (14) is displayed in Fig. 3(d) as a red dashed line. Most of the specular energy is confined around (14).

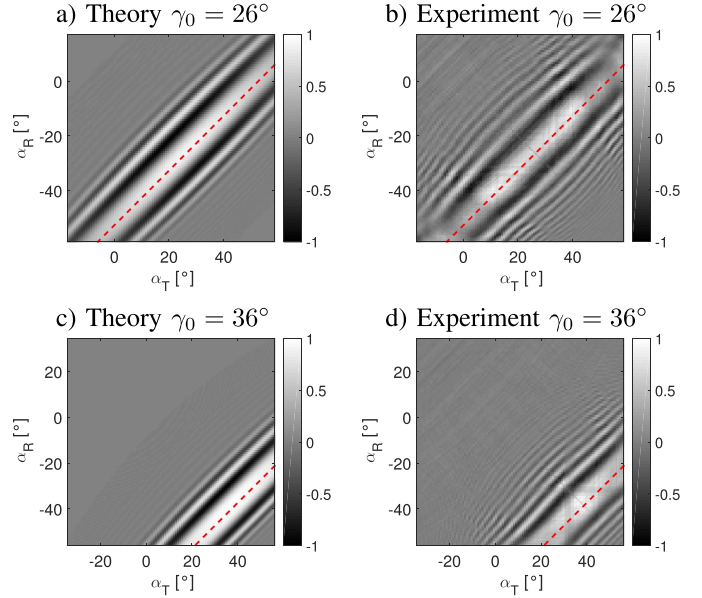


Fig. 5. Experimental validation of the proposed theory for $g(P, \alpha_T, \alpha_R)$ for a needle inserted in an Agar phantom. (a) Theory (11) for $\gamma_0 = 26^\circ$. (b) Experiment $\gamma_0 = 26^\circ$. (c) Theory (11) $\gamma_0 = 36^\circ$. (b) Experiment $\gamma_0 = 36^\circ$.

It is possible to exploit the coherence of the reflected signal along the (α_T, α_R) direction and design an adaptive apodization that maximizes the ratio between specular and diffusive energy. One way of accomplishing this is by compounding coherently all signals that verify (14), that is

$$f(P, \gamma) = \sum_{\forall \alpha_T} g(P, \alpha_T, \alpha_T - 2\gamma). \quad (16)$$

The result is a unidimensional signal expressed in terms of the orientation angle γ of the associated specular reflector. For similarity with the Hough transform [30], we call (16) the *specular transform*. As the Hough transform, the specular transform contains information on both the angle and the likelihood of finding a specular reflector at point P . Fig. 4 shows two examples of the specular transform of a signal received from a reflector, in this case a needle inserted into an Agar phantom, for inclinations $\gamma_0 = 26^\circ$ and $\gamma_0 = 36^\circ$.

E. Matched Filter Based for Specular Energy

If we neglect the influence of the element directivity, we can derive a model for the specular transform of a reflector with

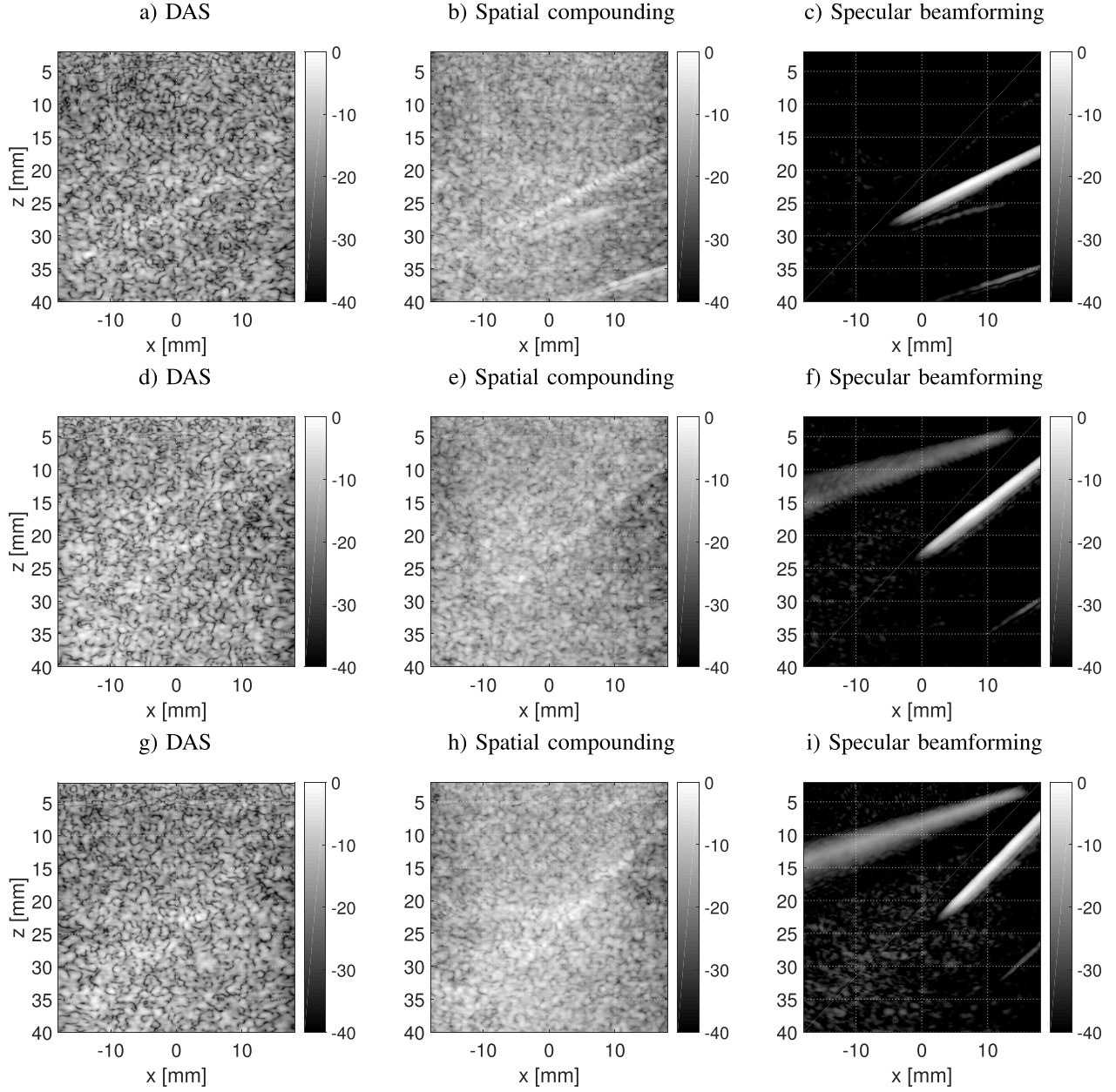


Fig. 6. Comparison of (a), (d), and (g) DAS, (b), (e), and (h) spatial compounding, and (c), (f), and (i) (21) for a 20G cannula inserted into an Agar phantom for the inclination of 26°, 36°, and 45°.

tilt γ_0 , namely

$$m(P, \gamma, \gamma_0) = e_{2W} \left(\frac{2z}{c_0} \left(\frac{1}{\cos(\gamma - \gamma_0)} - 1 \right) \right). \quad (17)$$

The derivation of (17) is included in Appendix A. Fig. 4 shows the evaluation of (17) for $P = (13, 19.6)$ mm and $\gamma_0 = 26^\circ$ and $P = (7, 17.5)$ mm and $\gamma_0 = 36^\circ$.

Equation (17) is a valid approximation for a wide variety of points and angles, but the approximation $S \equiv P$ is only true on the reflector interface. In addition, (17) is only valid for planar reflectors. Curved reflectors will show a different specular signature, still centered around (14) but spread over a wider area.

Equation (17) can be used as a matched filter that maximizes the output SNR and hence the probability of detection.

Since (17) is invariant to γ_0 , the matched filter can be implemented by correlating $f(P, \gamma)$ and $m(P, \gamma, 0)$. Let us write the normalized correlation operator as

$$r(P, \gamma) = \frac{\|f(P, \gamma) \star m(P, \gamma, 0)\|}{\sqrt{\mathcal{E}\{f(P, \gamma)\}\mathcal{E}\{m(P, \gamma, 0)\}}} \quad (18)$$

where \star denotes the correlation operation, and $\mathcal{E}\{\cdot\}$ denotes the energy of a signal. Expression (18) is energy correlated so as to provide an estimation of the similarity of both signals. The signal energy is of little interest; only the pulse shape carries information on the probability of having a reflector at P . If both signals are identical, then the maximum of $r(P, \gamma)$ will be 1, and less than that otherwise. It can therefore be used as detection parameter that, according to the matched filter theory, maximizes SNR. Let us denote this likelihood

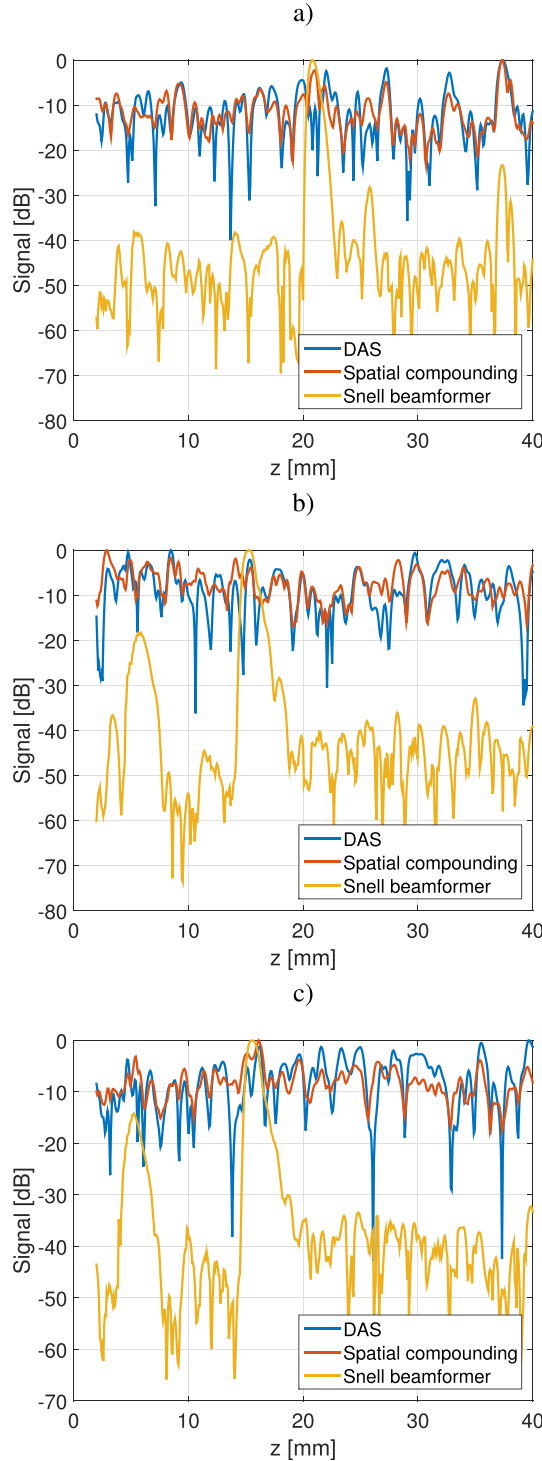


Fig. 7. Intensity levels at $x = 10$ mm for needles inclination. (a) 25° . (b) 36° . (c) 42° .

index by

$$\Lambda(P) = \max\{r(P, \gamma)\} \quad (19)$$

where max denotes the maximum operator. If in effect there is a reflector at P , then its inclination γ_0 can be estimated as

$$\gamma_0(P) = \arg \max\{r(P, \gamma)\} \quad (20)$$

where $\arg \max$ denotes the argument of the maximum operator. Figs. 15–17, in Appendix B, show the estimated maps of Λ and γ_0 in different scenarios.

Detection can be carried out directly on $\Lambda(P)$, and however, a more natural-looking ultrasound image can be generated using $\gamma_0(P)$ to define an adaptive transmit–receive apodization tailored to specular energy

$$b_{\text{SPEC}}(P) = \Lambda(P) \sum_{\forall \gamma} f(P, \gamma) \cdot \|m(P, \gamma, \gamma_0(P))\| \quad (21)$$

where we include $\Lambda(P)$ in the beamformer to improve target visibility.

III. MATERIALS AND METHODS

Experimental data were acquired with a Verasonics Vantage 256 scanner and the 128-elements L11 probe (Verasonics, Inc., Kirkland, WA, USA) using a 3.8-MHz transmit frequency and a 2.5 cycles long pulse. STA data sets were acquired in four *in vitro* scenarios:

- 1) a set of metal profiles immersed in deionized water;
- 2) an Agar phantom;
- 3) a 20G cannula inserted in an Agar phantom;
- 4) a 20G cannula inserted in a section of a pig's front leg.

The phantom was fabricated using 3% Agar, 0.3% Sephadex 25G (Sigma-Aldrich, St. Louis, MO, USA), and 96.7% ultrapure water (Milli-Q Direct, Merck Millipore, Billerica, MA, USA). The components were set into a beaker at room temperature and mixed with a magnetic stirrer. The mixture was heated to 90°C and kept at that temperature for 45 min. After that time, the mixture was let to cool down while stirring. Once it reached 50°C , the mix was poured into a rectangular mold ($60 \times 40 \times 100$ mm) and cured at room temperature for 24 h.

A section of a pig's front leg was used, containing the radius and ulna bones and adjacent tissues. The leg section was immersed in a water bath at room temperature. The cannula was inserted in different locations and with different incidence angles into the extensor carpi radialis.

For all cases, the acquired data were delayed and expressed in terms of α_T and α_R . The specular transform was computed with (16), and probability and angle maps were computed with (19) and (20). Specular images were then beamformed with (21). Conventional images were also produced with delay and sum (DAS) and spatial compounding using $\theta = [-15^\circ, 0^\circ, 15^\circ]$. In both cases, a transmit f -number of $F_T = 1.7$ and a receive f -number of $F_R = 1.2$ were used.

IV. RESULTS

The results in Fig. 5 validate the proposed theory. Equation (11) is compared with experimental data obtained with a needle inserted into an Agar phantom with two different orientations ($\gamma_0 = 26^\circ$ and $\gamma_0 = 36^\circ$). We observe a good match between theory and experiment. Equation (14) is also plotted as a red dashed line for reference.

Fig. 6 compares the needle detection performance of the specular beamformer against the state-of-the-art techniques. A 20G cannula was inserted into an Agar phantom with

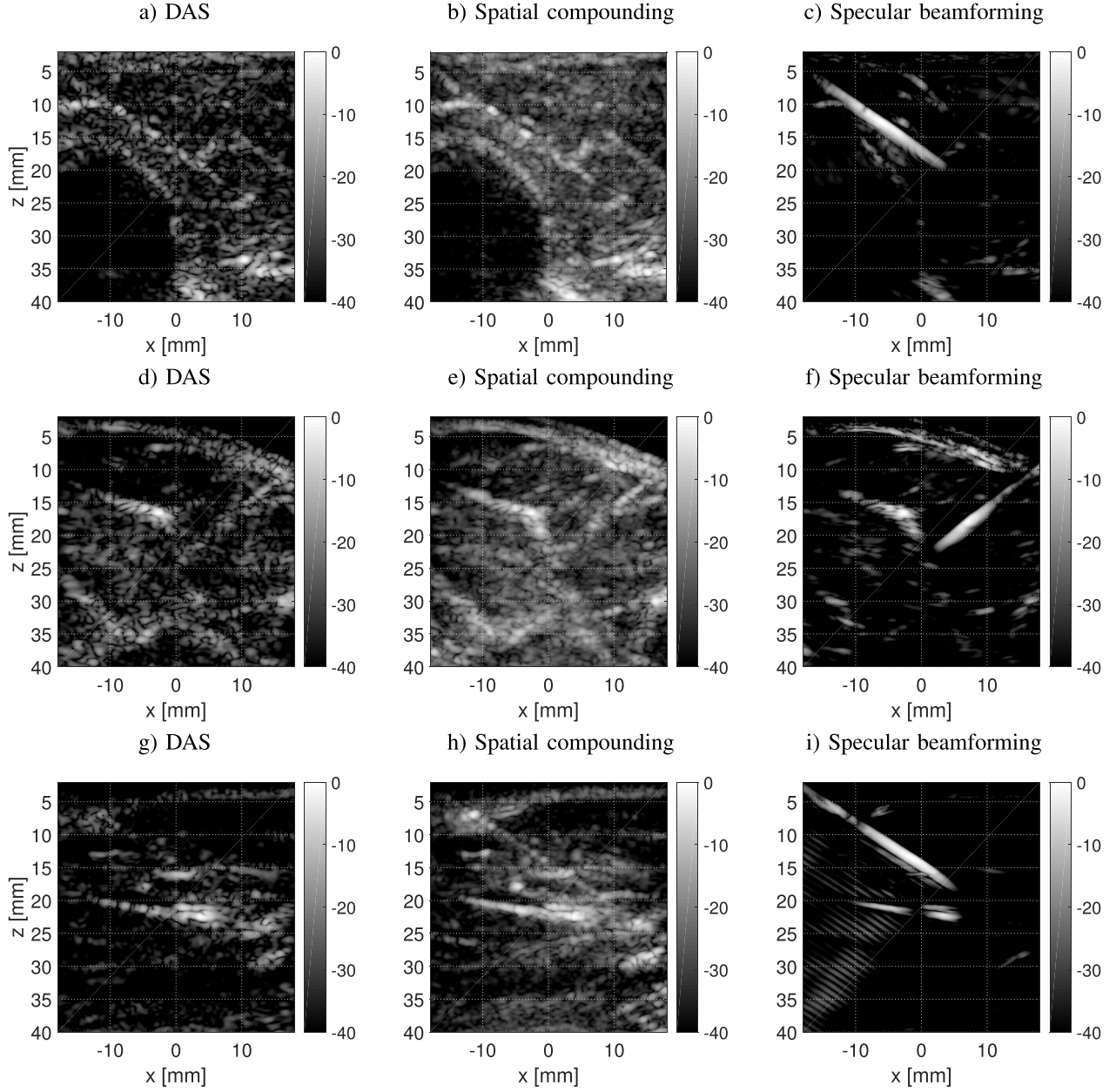


Fig. 8. Comparison of (a), (d), and (g) DAS, (b), (e), and (h) spatial compounding, and (c), (f), and (i) specular beamforming for a needle inserted in a pork leg.

inclinations: 26° , 36° , and 45° . Fig. 6(a), (d), and (g) shows the conventional DAS images. Fig. 6(b), (e), and (h) shows the spatial compounded images with tilting angles $\theta = [-15^\circ, 0^\circ, 15^\circ]$. Fig. 6(c), (f), and (i) shows the specular beamformed images using (21). The corresponding $\Lambda(P)$ and $\gamma_0(P)$ maps for the three inclinations are shown in Fig. 15 (Appendix B).

We observe that (21) outperforms the conventional techniques. The needle shaft is clearer in the specular beamformed images. The needle, however, is not visible all across the field of view. Only the section closer to the probe is displayed. This result was expected, since only specular energy is detected by (21).

In Fig. 6(f) and (i), we observe the grating lobes described in [5]. Grating lobes are also present in DAS and spatial

compounding images, but they lie below the speckle noise level in this case.

Fig. 7 compares the intensity level of the scan line at $x = 10$ mm for the three beamforming methods. The signal-to-speckle ratio is increased by 30–60 dB, depending on the needle angle. The ratio between signal and grating lobes stays between 15 and 20 dB.

Fig. 8 shows the performance of the specular beamformer on biological tissue. A 20G cannula was inserted into the extensor carpi radialis of a pig's front leg, in different locations and with different angles of incidence. Fig. 8(a), (d), and (g) shows the conventional DAS images. Fig. 8(b), (e), and (h) shows spatial compounded images. Fig. 8(c), (f), and (i) shows specular beamformed images. The corresponding $\Lambda(P)$ and $\gamma_0(P)$ maps for the three inclinations are shown in

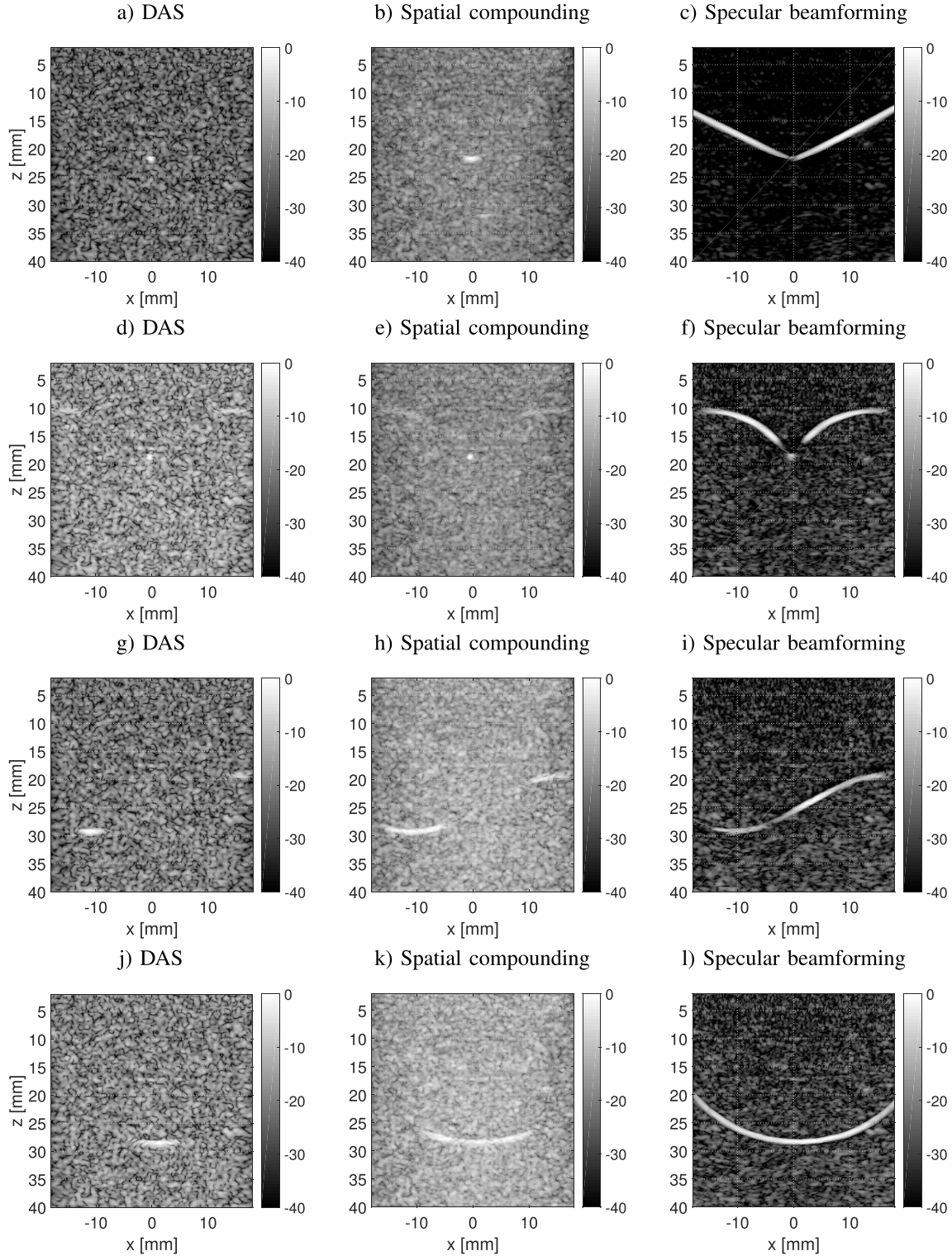


Fig. 9. Comparison of (a), (d), (g), and (j) DAS, (b), (e), (h), and (k) spatial compounding, and (c), (f), (i), and (l) specular beamforming for four metal profiles embedded into speckle noise.

Fig. 16 (Appendix B). As expected, needles are more easily visualized with the proposed technique. Other structures are also highlighted, presumably containing reflective energy.

To illustrate how the specular beamformer adapts to the reflector shape, the method was tested against complex shapes. Several metal profiles, containing curve and linear interfaces,

were immersed in deionized water, and STA data sets were recorded. An additional STA data set was acquired containing only speckle noise. The speckle noise data set was then added to the other data sets to simulate a controlled source of speckle noise. The combined data sets were beamformed with DAS, spatial compounding, and the specular beamformer. The resulting images are shown in Fig. 9.

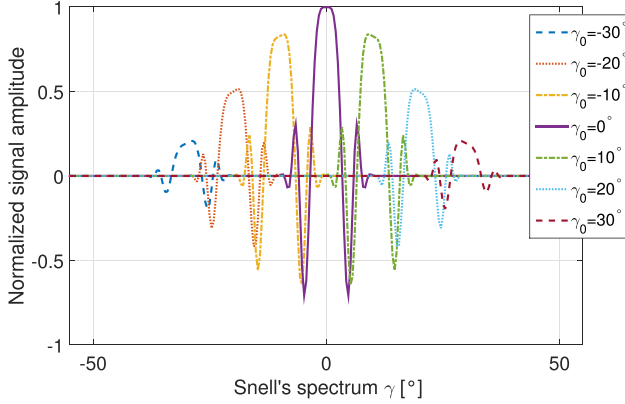


Fig. 10. Specular transform of the signal received from planar reflector with different orientations $\gamma_0 = [-30, -20, -10, 0, 10, 20, 30]^\circ$.

The reflecting interfaces are hardly visible with conventional DAS. Spatial compounding improves upon DAS, but large sections of the reflectors are still covered by speckle noise. Only those parts that are normal to the beam direction stick out from the background. Specular beamforming outperforms the two conventional methods, but its performance is hampered in curved interfaces. By inspecting the corresponding $\Lambda(P)$ maps, included in Fig. 17 (Appendix B), we observe that $\Lambda(P)$ drops in curved interfaces. This was expected since (11) was derived for planar reflectors.

V. DISCUSSION

By including the physics of specular reflection, the proposed beamformer makes it possible to visualize specular interfaces that are buried in speckle noise. But not all interfaces can be retrieved.

In Fig. 6, we observed that only the closest section of the needle was detected, specially for large tilting angles. This is a direct consequence of the law of reflection and a proof of the specificity of (21) for detecting specular energy. In order to receive any specular energy from a given reflecting point, there must be a combination of transmit and receive angles that fulfill the law of reflection. Otherwise, the pulse will be reflected away from the probe and no specular energy will be detected. This sets a limit to what we can detect; some regions of the needle will never reflect specular energy back to the probe.

This limitation can only be addressed by increasing the probe aperture, or even better, by using a concave aperture surrounding the area of interest. This solution is, however, impractical in many situations, due to both cost and ergonomic reasons. A small pitch is desirable, in the order of $\lambda/2$, to enable the use of steep incidence angles and to eliminate grating lobes.

For the visualization of reflectors, it may be beneficial to use a lower frequency than the one conventionally used for scattering tissue. A possible solution would be a combined operation mode: two images are produced using two different frequencies and the images are then combined using a priority mask. Alternatively, for instance in needle tracking

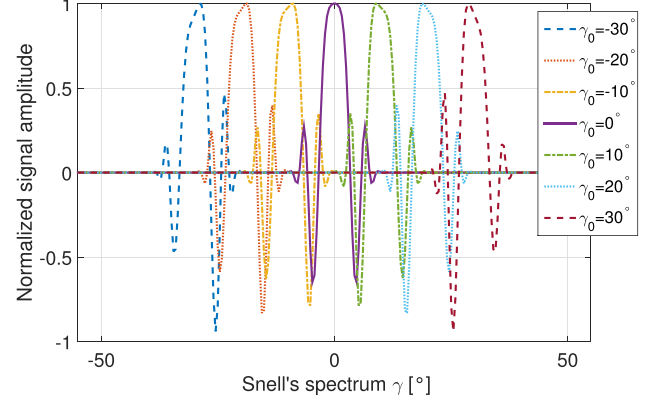


Fig. 11. Amplitude normalized specular transform of the signal received from planar reflector with different orientations $\gamma_0 = [-30, -20, -10, 0, 10, 20, 30]^\circ$.

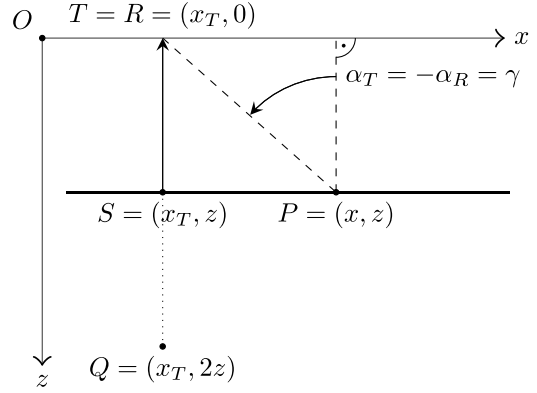


Fig. 12. Geometrical entities used for delay calculation in the presence of a planar reflector at B with inclination $\gamma_0 = 0$.

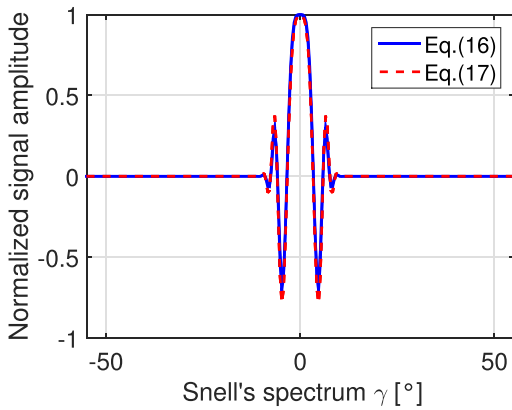
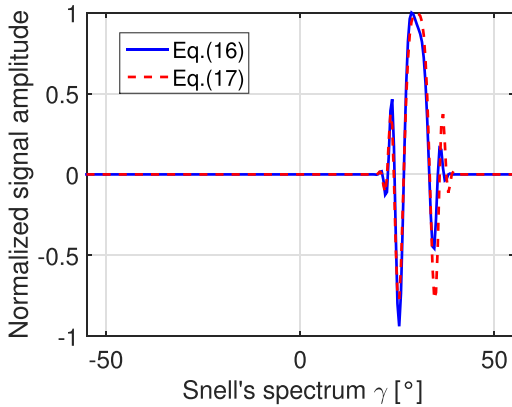
applications, one can detect the needle attitude on the specular image and draw a line on top of the scattering image.

The third dimension also poses a challenge. While only 2-D reflecting interfaces were tackled here, most specular objects are 3-D. In many cases, if a 1-D array is used, the transmitted pulse will be reflected outside of the imaging plane, and then, the specular energy becomes undetectable. This could be addressed with the 3-D imaging technology. However, fully addressable 2-D arrays are still rare.

The algorithm leaves also room for improvement. The results presented here are based on the assumption $P \equiv S$, which reduces the resolution of the $\Lambda(P)$ map. The model could be expanded to curved reflectors improving the detection of complex geometries.

It must be noted that the reported improvement in SNR could be misleading. As recently pointed out in [31], any statement on the improvement of contrast becomes invalid if the tested algorithm alters the dynamic range of the input signal. The presented algorithm certainly does so. Therefore, the reported SNR values could be overly optimistic. It seems beyond doubt that the algorithm increases SNR: we observe a signal whose level was originally below the speckle noise level. But, a test for specular interfaces must be defined to calibrate the SNR improvement.

The implementation used here is not real time. Each specular image was produced in about 2 min using a combination

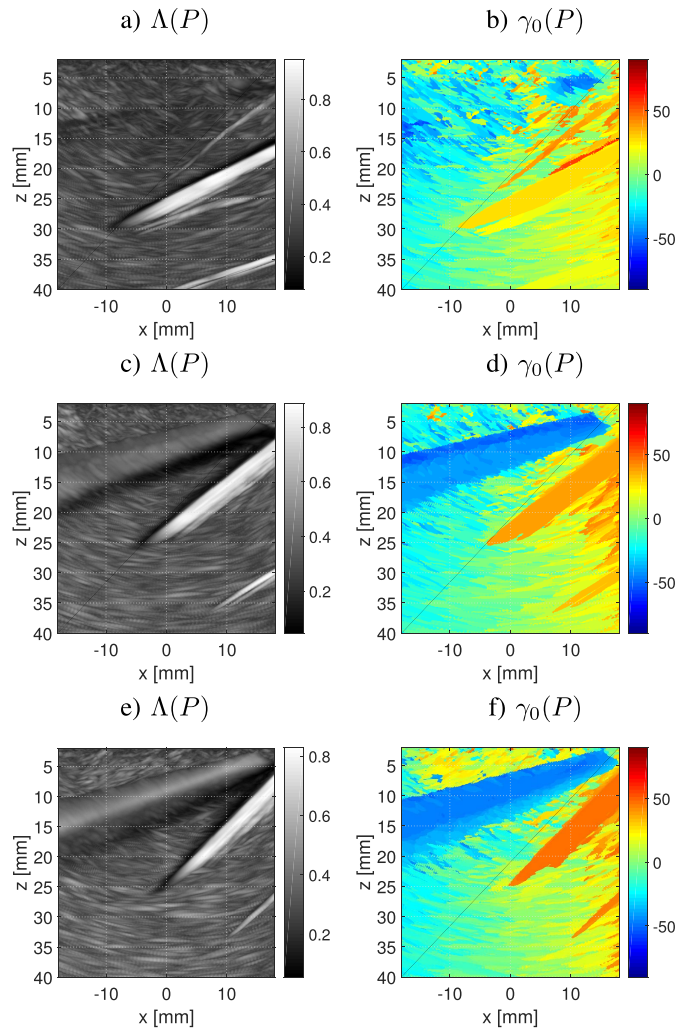
Fig. 13. Comparison of (11) and (17) for $\gamma_0 = 0^\circ$.Fig. 14. Comparison of (11) and (17) for $\gamma_0 = 30^\circ$.

of C++ and MATLAB code on a conventional workstation. About half of the time was used to calculate the specular transform $f(P, \gamma)$, and the rest for the matched filter. The implementation can be accelerated. The delayed signal $g(P, \alpha_T, \alpha_R)$ can be computed and processed pixel by pixel, rather than computing the full $g(P, \alpha_T, \alpha_R)$ map for all pixels at once. That will reduce the amount of RAM needed and avoid memory swapping. The algorithm is easily parallelizable and can benefit from a GPU implementation. Finally, the number of operations can be substantially reduced using other imaging sequences, such as coherent plane-wave compounding or diverging waves, and by accepting some simplifications in the implementation of the matched filter.

VI. CONCLUSION

We present an adaptive beamforming algorithm based on the law of reflection. The signal is expressed in terms of the transmit and receive angles and transformed to the space of angles that verify the law of reflection, a so-called specular domain. If in effect the signal has been reflected by a specular interface, its energy will be concentrated around a value γ_0 in the specular domain that corresponds to the inclination of the reflector.

Moreover, by combining the image source principle and the linear impulse response theory, we derive a model for the signal reflected from a planar interface. That theory is used to implement a matched filter that maximizes the signal-to-speckle noise ratio and hence detection probability.

Fig. 15. Estimated $\Delta(P)$ and $\gamma_0(P)$, in degrees, for a 20G cannula inserted in an Agar phantom with different inclination. (a) and (b) $\Delta(P)$ and $\gamma_0(P)$ for 26° , (c) and (d) $\Delta(P)$ and $\gamma_0(P)$ for 36° , (e) and (f) $\Delta(P)$ and $\gamma_0(P)$ for 45° .

In vitro results suggest that the proposed algorithm improves the visualization of reflecting interfaces, increasing in 30–60 dB, the signal-to-speckle noise ratio. Promising results are obtained in biological tissue for the application of needle visualization.

Further research is needed to extend the proposed theory to curvilinear interfaces. Work must also be done to increase the range of directions that can be detected, something that may require new probe geometries tailored to the visualization of specular interfaces.

APPENDIX A DERIVATION OF THE SPECULAR MATCHED FILTER MODEL

Fig. 10 shows the evaluation of (16) for several planar reflectors, all placed at $P = (0, 20)$ mm but with inclination ranging from -30° to 30° . For this simulation, a 128 elements, 300 μm pitch, linear array centered at the origin was used with a 5.2-MHz center frequency. We observe that $f(P, \gamma)$ has a similar shape for all orientations.

In order to design a matched filter for the specular energy in $f(P, \gamma)$, the absolute values of the signal for a given

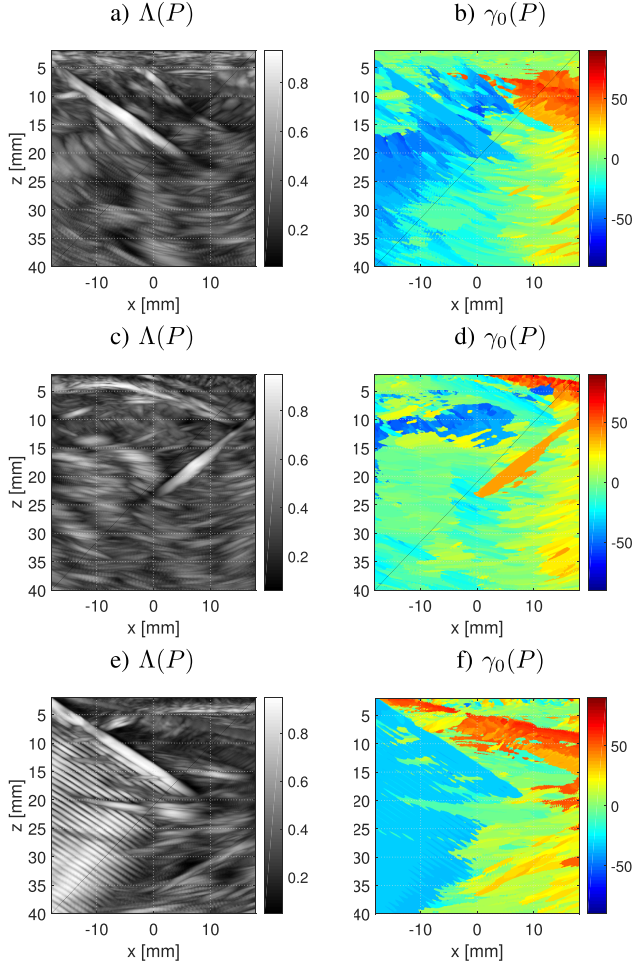


Fig. 16. Estimated $\Delta(P)$ (a, c, e) and $\gamma_0(P)$ (b, d, f), in degrees, for three cases of a 20G cannula inserted into a pig's front leg.

orientation are unimportant; the absolute amplitude does not carry additional information on the probability of finding a reflector at P . It is the pulse shape that does. Therefore, it is possible to normalize the transformed signal in amplitude. Furthermore, if we neglect the effect of the element directivity, the similarity between the pulses becomes evident, as shown in Fig. 11.

It is possible to derive a model for the particular case of $\gamma_0 = 0$ and then extend the model to other reflector orientations by convolving the model with $\delta(\gamma - \gamma_0)$.

We set a planar reflector at depth z and the focal point at $P = (x, z)$, as shown in Fig. 12. We previously observed that $g(P, \alpha_T, \alpha_R)$ is nearly symmetric respect to $\alpha_T = \alpha_R + 2\gamma_0$. Particularly for $\gamma_0 = 0$, $g(P, \alpha_T, \alpha_R)$ is symmetric respect to $\alpha_T = \alpha_R$.

Therefore, it suffices to investigate $g(P, \alpha_T, \alpha_R)$ over the line $\alpha_T = -\alpha_R$, i.e., the perpendicular to the symmetry axis. On that axis, both T and R lie on the same location, as shown in Fig. 12. The location of the image source Q is $(x_T, 2z)$, and hence, $|QR| = 2z$. The focusing distance is

$$|\vec{TP}| + |\vec{PR}| = 2\sqrt{z^2 + (x - x_T)^2} \quad (22)$$

which can be expressed in terms of α_T as

$$|\vec{TP}| + |\vec{PR}| = 2z\sqrt{1 + \tan^2 \alpha_T} = \frac{2z}{\cos \alpha_T}. \quad (23)$$

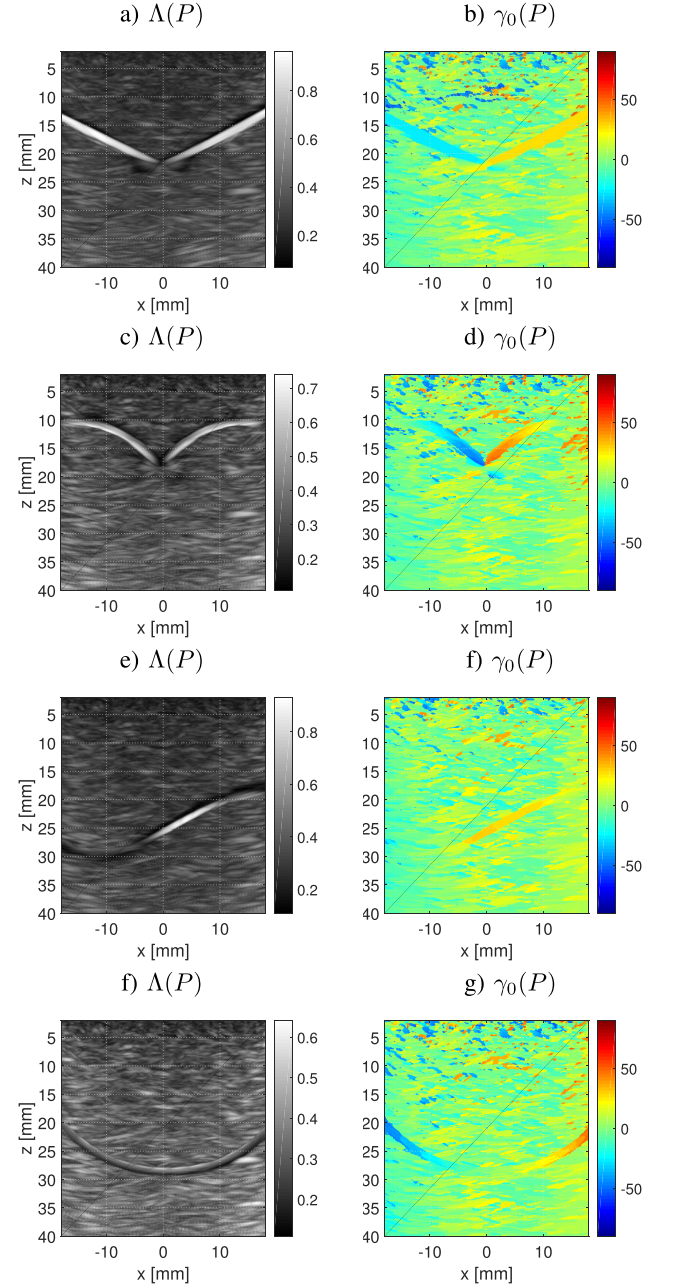


Fig. 17. Estimated $\Delta(P)$ (a, c, e, f) and $\gamma_0(P)$ (b, d, f, g), in degrees, for four metal profiles and speckle noise.

Neglecting the directivity and geometric dispersion in (11), the value of the delayed pulse-echo signal at P along the axis $\alpha_T = -\alpha_R$ becomes

$$g(P, \alpha_T, -\alpha_T)|_{\gamma_0=0} \approx e_{2W} \left(\frac{2z}{c_0} \left(\frac{1}{\cos \alpha_T} - 1 \right) \right). \quad (24)$$

Notice that if $\alpha_T = 0$, then $g(P, \alpha_T, -\alpha_T)|_{\gamma_0=0} \approx e_{2W}(0)$ and perfect reflection occurs. Applying the transformation (16) to (24), we find that

$$\alpha_T = -\alpha_r = -\alpha_T + 2\gamma \iff \alpha_T = \gamma \quad (25)$$

and the specular transform of (24) yields

$$f(P, \gamma)|_{\gamma_0=0} \approx e_{2W} \left(\frac{2z}{c_0} \left(\frac{1}{\cos \gamma} - 1 \right) \right) \quad (26)$$

which can be taken as a model for $f(P, \gamma)$ if $\gamma_0 = 0$. This model can be extended to other reflector orientations by convolving (26) by $\delta(\gamma - \gamma_0)$ yielding (17). Figs. 13 and 14 compare the derived model (17) with the theoretical signal (11).

APPENDIX B PROBABILITY AND ANGLES MAPS

Fig. 15 shows the probability $\Lambda(P)$ and inclination $\gamma_0(P)$ maps for a needle inserted in an Agar phantom. Fig. 16 shows the $\Lambda(P)$ and $\gamma_0(P)$ maps for a needle inserted in biological tissue. Fig. 17 shows the $\Lambda(P)$ and $\gamma_0(P)$ maps for several metal reflectors in the speckle noise.

REFERENCES

- [1] R. F. Wagner, S. W. Smith, J. M. Sandrik, and H. Lopez, "Statistics of speckle in ultrasound B-scans," *IEEE Trans. Sonics Ultrason.*, vol. SU-30, no. 3, pp. 156–163, May 1983.
- [2] I. Hacihaliloglu, R. Abugharbieh, A. J. Hodgson, and R. N. Rohling, "Bone surface localization in ultrasound using image phase-based features," *Ultrasound Med. Biol.*, vol. 35, no. 9, pp. 1475–1487, 2009.
- [3] K. J. Chin, A. Perlas, V. W. S. Chan, and R. Brull, "Needle visualization in ultrasound-guided regional anesthesia: Challenges and solutions," *Regional Anesthesia Pain Med.*, vol. 33, no. 6, pp. 532–544, 2008.
- [4] I. Hacihaliloglu, "Towards a novel minimally invasive 3D ultrasound imaging based computer assisted orthopaedic surgery system for bone fracture reduction," Ph.D. dissertation, Dept. Elect. Comput. Eng., Univ. Brit. Columbia, Vancouver, BC, Canada, 2010, p. 2.
- [5] A. Rodriguez-Molares, L. Løvstakken, I. K. Ekroll, and H. Torp, "Needle detection by image source localization," in *Proc. IEEE Int. Ultrason. Symp. (IUS)*, Oct. 2015, pp. 1–4.
- [6] D. V. Amin, T. Kanade, A. M. Digioia, and B. Jaramaz, "Ultrasound registration of the bone surface for surgical navigation," *Comput. Aided Surgery*, vol. 9, no. 1, pp. 1–16, 2003.
- [7] K. J. Chin, A. Perlas, V. Chan, D. Brown-Shreves, A. Koshkin, and V. Vaishnav, "Ultrasound imaging facilitates spinal anesthesia in adults with difficult surface anatomic landmarks," *Anesthesiology*, vol. 115, no. 1, pp. 94–101, 2011.
- [8] S.-W. Chan, "Emergency bedside ultrasound for the diagnosis of rib fractures," *Amer. J. Emerg. Med.*, vol. 27, no. 5, pp. 617–620, 2009.
- [9] P. M. Novotny *et al.*, "GPU based real-time instrument tracking with three-dimensional ultrasound," *Med. Image Anal.*, vol. 11, no. 5, pp. 458–464, 2007.
- [10] D. B. Williams *et al.*, "Endoscopic ultrasound guided fine needle aspiration biopsy: A large single centre experience," *Endoscopy*, vol. 44, no. 5, pp. 720–726, 1999.
- [11] P. Marhofer and V. W. S. Chan, "Ultrasound-guided regional anesthesia: Current concepts and future trends," *Anesthesia Analgesia*, vol. 104, no. 5, pp. 1265–1269, 2007.
- [12] C. H. Rodeck, C. A. Holman, J. Karnicki, J. R. Kemp, D. N. Whitmore, and M. A. Austin, "Direct intravascular fetal blood transfusion by fetoscopy in severe rhesus isoimmunisation," *Lancet*, vol. 317, no. 8221, pp. 625–627, 1981.
- [13] P. M. Shankar, "Speckle reduction in ultrasound B-scans using weighted averaging in spatial compounding," *IEEE Trans. Ultrason., Ferroelect., Freq. Control*, vol. 33, no. 6, pp. 754–758, Nov. 1986.
- [14] R. R. Entrekkin, B. A. Porter, H. H. Sillesen, A. D. Wong, P. L. Cooperberg, and C. H. Fix, "Real-time spatial compound imaging: Application to breast, vascular, and musculoskeletal ultrasound," *Seminars Ultrasound, CT MRI*, vol. 22, no. 1, pp. 50–64, 2001.
- [15] D. C. Lin *et al.*, "Advantages of real-time spatial compound sonography of the musculoskeletal system versus conventional sonography," *Amer. J. Roentgenol.*, vol. 179, no. 6, pp. 1629–1631, 2002.
- [16] J. F. Synnevag, A. Austeng, and S. Holm, "Adaptive beamforming applied to medical ultrasound imaging," *IEEE Trans. Ultrason., Ferroelect., Freq. Control*, vol. 54, no. 8, pp. 1606–1613, Aug. 2007.
- [17] I. K. Holfort, F. Gran, and J. A. Jensen, "High resolution ultrasound imaging using adaptive beamforming with reduced number of active elements," *Phys. Procedia*, vol. 3, no. 1, pp. 659–665, 2010.
- [18] Z. Wang, J. Li, and R. Wu, "Time-delay- and time-reversal-based robust Capon beamformers for ultrasound imaging," *IEEE Trans. Med. Imag.*, vol. 24, no. 10, pp. 1308–1322, Oct. 2005.
- [19] S. Mehdizadeh, A. Austeng, T. F. Johansen, and S. Holm, "Eigenspace based minimum variance beamforming applied to ultrasound imaging of acoustically hard tissues," *IEEE Trans. Med. Imag.*, vol. 31, no. 10, pp. 1912–1921, Oct. 2012.
- [20] S. Kidera, T. Sakamoto, and T. Sato, "Accurate UWB radar three-dimensional imaging algorithm for a complex boundary without range point connections," *IEEE Trans. Geosci. Remote Sens.*, vol. 48, no. 4, pp. 1993–2004, Apr. 2010.
- [21] D. Tran and R. N. Rohling, "Automatic detection of lumbar anatomy in ultrasound images of human subjects," *IEEE Trans. Biomed. Eng.*, vol. 57, no. 9, pp. 2248–2256, Sep. 2010.
- [22] R. S. Bandaru, A. Sørnes, J. D'hooge, and E. Samset, "2D localization of specular reflections using ultrasound," in *Proc. IEEE IUS*, Chicago, IL, USA, Sep. 2014, pp. 2209–2212.
- [23] A. Rodriguez-Molares, L. Løvstakken, I. K. Ekroll, and H. Torp, "Reconstruction of specular reflectors by iterative image source localization," *J. Acoust. Soc. Amer.*, vol. 138, no. 3, p. 1365, 2015.
- [24] A. Rodriguez-Molares, A. Fatemi, H. Torp, and L. Løvstakken, "Adaptive beamforming based on Snell's law of reflection," in *Proc. IEEE Int. Ultrason. Symp. (IUS)*, Sep. 2016, pp. 1–4.
- [25] M. Karaman, P.-C. Li, and M. O'Donnell, "Synthetic aperture imaging for small scale systems," *IEEE Trans. Ultrason., Ferroelect., Freq. Control*, vol. 42, no. 3, pp. 429–442, May 1995.
- [26] G. Montaldo, M. Tanter, J. Bercoff, N. Benach, and M. Fink, "Coherent plane-wave compounding for very high frame rate ultrasonography and transient elastography," *IEEE Trans. Ultrason., Ferroelect., Freq. Control*, vol. 56, no. 3, pp. 489–506, Mar. 2009.
- [27] J. Kortbek, J. A. Jensen, and K. L. Gammelmark, "Sequential beamforming for synthetic aperture imaging," *Ultrasonics*, vol. 53, no. 1, pp. 1–16, 2013.
- [28] H. Hasegawa and H. Kanai, "High-frame-rate echocardiography using diverging transmit beams and parallel receive beamforming," *J. Med. Ultrason.*, vol. 38, no. 3, pp. 129–140, 2011.
- [29] P. R. Stepanishen, "Transient radiation from pistons in an infinite planar baffle," *J. Acoust. Soc. Amer.*, vol. 49, no. 5B, p. 1629–1638, 1971.
- [30] R. O. Duda and R. E. Hart, "Use of the Hough transformation to detect lines and curves in pictures," *Commun. ACM*, vol. 15, no. 1, pp. 11–15, Jan. 1972.
- [31] O. M. H. Rindal, A. Austeng, H. Torp, S. Holm, and A. Rodriguez-Molares, "The dynamic range of adaptive beamformers," in *Proc. IEEE Int. Ultrason. Symp. (IUS)*, Sep. 2016, pp. 1–4.



Alfonso Rodriguez-Molares received the M.Sc. degree in telecommunications and the Ph.D. degree in signal processing and communication from the University of Vigo, Vigo, Spain, in 2006 and 2011, respectively.

He is currently a Senior Engineer with the Ultrasound Laboratory, Norwegian University of Science and Technology, Trondheim, Norway. He has coauthored over 10 papers in peer-reviewed journals, and holds two patents. His current research interests include medical ultrasound, adaptive beamforming, acoustic propagation in heterogeneous media, and numerical acoustics.



Ali Fatemi received the M.Sc. degree in medical technology from the Norwegian University of Science and Technology, Trondheim, Norway, in 2015, where he is currently pursuing the Ph.D. degree with the Department of Circulation and Medical Imaging, with a focus on the application of adaptive beamforming to cardiac ultrasound.



Lasse Løvstakken received the M.Sc. degree in engineering cybernetics and the Ph.D. degree in medical ultrasound imaging technology from the Norwegian University of Science and Technology (NTNU), Trondheim, Norway,

He is currently a Professor with the Department of Circulation and Medical Imaging, NTNU. His current research interests include signal and image processing applied in medical ultrasound imaging for improved image formation and the detection and estimation of moving tissue and blood flow, and cardiovascular imaging with emphasis on methods for improved estimation of blood velocities in the heart and vessels.



Hans Torp received the M.Sc. and Dr.Techn. degrees from the Norwegian University of Science and Technology (NTNU), Trondheim, Norway, in 1978 and 1992, respectively.

He is currently a Professor and the Head of the Ultrasound Research Group with the Department of Circulation and Medical Imaging, NTNU. He has more than 35 years of experience in research and development within medical ultrasound technology. He has co-supervised 16 Ph.D. students and over 20 students. He has coauthored 107 papers in peer-reviewed journals, and holds approximately 40 patents (24 of them granted). His current research interests include stochastic signal/image processing with applications in ultrasonic imaging, Doppler, and color flow imaging.